

SAND80-1434  
Unlimited Release

Quasi-Static and Creep Data for Dome Salt From Bryan Mound, Texas

W. R. Wawersik  
D. J. Holcomb  
D. W. Hannum  
H. S. Lauson  
Sandia National Laboratories  
Albuquerque, New Mexico 87185

Abstract

Experiments are described for quasi-static loading conditions and for creep at zero, 500 (3.5) and 2000 (13.8 MPa) psi confining pressure and at 22 and 60°C. All quasi-static test results were consistent with data from other sources including unconfined and **triaxial** compressive strengths, ultimate strains, secant moduli during first laboratory loading and elastic constants. In contrast, creep of Bryan Mound salt was anomalous in that the observed creep rates were one to two orders of magnitude smaller than the typical creep rates of other rock salt of similar purity subjected to the same conditions of stress and temperature. No temperature effect was resolved on creep of Bryan Mound salt within the scatter of the data. Comparative data for triaxial compression and extension suggest reductions in the failure strains and changes in the failure modes with increasing intermediate principal stress. These effects are attributed to differences in microfracture networks. Microfracturing was observed optically and indirectly by measuring acoustic emissions. The acoustic emissions correlated directly with the magnitude of the observed volumetric strain.

## Table of Contents

	<u>Page</u>
List of Symbols and Conventions .....	iii
List of Tables .....	iv
List of Figures .....	v
Introduction .....	1
Site and Sample Description .....	1
Sample Preparation .....	3
Apparatus and Experimental Procedures .....	3
Strength/Deformation Experiments .....	3
Acoustic Emission Measurements .....	5
Data Reduction .....	6
Test Matrix .....	8
Experimental Results .....	11
Quasi-Static Tests .....	11
Creep Experiments .....	17
Acoustic Emissions .....	22
Summary and Conclusions .....	22
References .....	25

### List of Symbols and Conventions

$\sigma_1, \sigma_2, \sigma_3$	True principal stresses ( <b>force</b> )/( <b>current</b> area)--compression positive
$\epsilon_1, \epsilon_2, \epsilon_3$	Engineering strains (change of <b>length</b> )/(original <b>length</b> )--contraction positive
$e_1, e_2, e_3$	<b>Natural</b> or logarithmic strains (change in <b>length</b> )/(current <b>length</b> )
$\gamma = e_1 - e_3$	Shear strain
$e = e_1 + e_2 + e_3$	Volumetric strain
$e_x$	Strain parallel to cylinder axis (axial strain)
$\delta$	Displacement
$(\sigma_1 - \sigma_3)_u$	Ultimate or maximum principal stress difference
$(e_1)_u, (e_3)_u, e_u$	Natural strain values corresponding to $(\sigma_1 - \sigma_3)_u$
$\Delta e_1, \Delta e_2, \Delta e_3$	Finite stress and strain increments
$E_s$	Secant modulus
$E, \nu, \mu$	Elastic constants (Young's modulus, Poisson's ratio and shear modulus)

The bulk of the data is expressed in English units consistent with SPR project requests.

## List of Tables

- Table I: **Summary** of Ultrasonic Velocity Measurements Prior to Laboratory Testing
- Table II: Test Matrix
- Table III: Maximum Stresses and Strains in Quasi-Static Tests
- Table IV: Summary of Secant Moduli of Bryan Mound Salt Upon First Laboratory Loading and List of Elastic Constants
- Table V: Average Dynamic Elastic Constants for Rock Salt From Drillholes **107A, 107C, 108B and 109A**
- Table VI: Summary of Data From Creep Experiments
- Table VII: Fitting Parameters for Axial Creep Strains,  $e_x$ .  $e_x = e_{x0} + e_{xa}$ .  
 $(1 - \exp(-\frac{t}{\tau})) + \dot{e}_{xs}t$  -- (time  $t$  in seconds)

## List of Figures

- Figure 1: Rock Salt From Bryan Mound Dome With Steeply Dipping Anhydrite Rich Bands Accentuated by Back-Illumination.
- Figure 2: Schematic of Sandia Triaxial Apparatus Showing Reference Points A, B for Axial Displacement Measurement  $\delta$ .
- Figure 3: Quasi-Static Unisxial Compression Data at 22°C, Core From Drillholes 107A, 109A and 108B.
- Figure 4: Quasi-Static Uniaxial Compression Data at 60°C,  $(\sigma_1 - \sigma_3)$  vs.  $e_1$ . Core From Drillholes 107A, 107C and 109A.
- Figure 5: Quasi-Static Unisxial Compression Data at 60°C,  $(\sigma_1 - \sigma_3)$  vs.  $\gamma$ . Core From Drillholes 107A, 107C and 109A.
- Figure 6: Quasi-Static Uniaxial Compression Data at 60°C,  $\gamma$  vs.  $e$ . Core From Drillholes 107A, 107C and 109A.
- Figure 7: Quasi-Static Triaxial Compression Data at 22°C,  $(\sigma_1 - \sigma_3)$  vs.  $\gamma$ . Core From Drillholes 107A and 108B. Strain Data for Q/108B-3316.5/0.5/22 Averaged From Dilatometric and Disk Gauge Measurements.
- Figure 8: Quasi-Static Triaxial Compression Data at 22°C,  $(\sigma_1 - \sigma_3)$  vs.  $e$ . Core From Drillholes 107A and 108B. Strain Data for Q/108B-3316.5/0.5/22 Averaged From Dilatometric and Disk Gauge Measurements.
- Figure 9: Quasi-Static Triaxial Compression Data at 22°C,  $\gamma$  vs.  $e$ . Core From Drillholes 107A and 108B. Strain Data for Q/108B-3316.5/0.5/22 Averaged From Dilatometric and Disk Gauge Measurements.
- Figure 10: Quasi-Static Compression and Extension Data at 22°C,  $(\sigma_1 - \sigma_3)$  vs.  $\gamma$ . Core From Drillhole 109A.
- Figure 11: Quasi-Static Compression and Extension Data at 22°C,  $(\sigma_1 - \sigma_3)$  vs.  $e$ . Core From Drillhole 109A. Volumetric Strain Data at  $\sigma_3 = 2000$  psi Questionable.
- Figure 12: Quasi-Static Compression and Extension Data at 22 and 60°C. Core From Drillhole 109A.
- Figure 13: Deformed Specimen after Triaxial Extension Creep Experiment at  $\sigma_3 = 2000$  psi,  $(\sigma_1 - \sigma_3) = 3020$  psi and 60°C (Test CE/107A-3965/2.0/60).
- Figure 14: Creep Data in Triaxial Compression and Extension at  $(\sigma_1 - \sigma_3) \approx 3000$  psi and at 22°C and 60°C,  $|e_x|$  vs. Time. Core From Drillholes 107A and 107C.

List of Figures (cont.)

- Figure 15: Creep Data in Trisxial Compression and Extension at  $(\sigma_1 - \sigma_3) \approx 3000$  psi at 22 and 60°C,  $\epsilon$  vs. Time. Core From Drillholes 107A and 107C.
- Figure 16: Principal Stress Difference vs. Acoustic Emissions in Trisxial Compression Test.
- Figure 17: Acoustic Emission Activity vs. Volumetric Strain During Test of Figures 7 and 16. Radial Strain Data Based on Disk Gauge Measurements Only.

## Introduction

Mechanical properties of rock salt from the Bryan Mound dome are needed for the design of twelve new crude oil storage caverns of the U. S. Strategic Petroleum Reserve (SPR) program. Tests on Bryan Mound material are part of a larger experimental effort to 1) establish the response of rock salt from different SPR sites, 2) incorporate the results of experiments into existing constitutive models, 3) assess the fracture potential of rock salt adjacent to the caverns and 4) establish a likely correspondence between acoustic emission and rock salt fracture. In this report, a summary is given of nineteen tests in quasi-static compression and in creep. Quasi-static tests were conducted at zero, 500 and 2000 psi (0, 3.5, 13.8 MPa) confining pressure. Creep experiments were carried out at 2000 psi (13.8 MPa) confining pressure. Both groups of tests included triaxial compression and triaxial extension experiments at 22 and 60°C.

## Site and Sample Description

The Bryan Mound dome is located in Brazoria County, Texas, two miles SSW of Freeport and one half mile off the Gulf of Mexico. No geological description of the dome was available. However, verbal information and a contour map indicate that the dome has a nearly circular horizontal cross section with an almost flat top at 1000 to 1200 ft (312-375 m) depth below surface. The dome diameter at 1200 ft (375 m) depth is approximately 5500 ft and increases to 7000 ft (2030 m) at a depth of 4500 ft (1400 m). The smallest and steepest average dip angles of the flanks appear to be 75° and 85° in the north and south, respectively.

Core was tested from four drillholes designated drillholes 107A, 107C, 108B and 109A at three prospective cavern sites which are located at least 1300 ft (406 m) from the flanks of the dome. Raw core diameters were 4 inches (10 cm)

throughout. The core depth varied from 2346 ft to 3964 ~~ft~~ (733-1239 m). However, because of the flow history of salt domes, depth is almost ~~un~~-related to salt stratigraphy. Grain size varied between 0.08 in (2 mm) and 1.6 in (40 mm). Available core from drillhole 109A had the most uniform grain size with an average of 0.3 in (8 mm), and it was free from large crystals exceeding 0.6 in (15 mm), had a very uniform light gray color and exhibited no preferred fabric. Material from drillhole 108B was fine to very coarse **grained** (grain size 0.04 to 0.6 in or 1 mm to 15 mm) with a mean grain size of 0.3 in (8 mm). Some of the 108B core contained 0.08-0.2 in (2-5 mm) wide, steeply dipping bands of dark, anhydritic salt at angles of 5 to 15° from vertical. The distance between these bands ranged from 0.2 in to 2 in (5-50 mm). Grains were elongated parallel to the dip and to the strike of the anhydritic bands. The strongest elongation along the dip of the bands produced grain axis ratios of 1.7 to 2.5.

Salt from drillholes 107A and 107C was similar to 108B material in that it had a rather nonuniform grain size ranging from 0.08 in (2 mm) to more than 1 in (25 mm). Large subhedral crystals were common. Both sets of core appeared to be relatively shattered, showed frequent cleavage and proved to be difficult to machine. Most of the **core from drillhole 107C** also contained dark, steeply dipping, anhydrite rich bands which were similar to but much more pronounced than those in the core of 108B. Banded and almost pure salt from **drillholes 107C** and 108B are compared in Fig. 1.

Chemical and mineralogical data were available only for material from another drillhole, hole **#109B** (1). This material had a density of 2.17 g/cc and contained approximately 93% of sodium chloride and up to 6% anhydrite. Based on the gradations of color from light to very dark gray in other core, it is assumed that the foregoing values are representative for all rock salt



which was evaluated in this series of experiments. Details of the compositions of core 109B and more recent data for material from other **drillholes** will be discussed elsewhere.

Additional core characterizations were conducted by means of ultrasonic velocity measurements in three directions parallel and perpendicular to the core axes. Measurements were made along two diameters, approximately normal and parallel to the strike of the preferred fabric directions. The data obtained are listed in Table I and indicate a slight material anisotropy in some specimens.

#### Sample Preparation

All tests were performed on right circular cylinders. The specimens were obtained by cutting the raw core to length on a band saw (7.25 to 8.25 in; 18.4 to 21.0 cm) and by finishing the ends on a surface grinder or, preferably, on a lathe. The end faces were held flat and parallel to  $\pm 0.001$  in. (0.025 mm). Alternatively, 3.5 in. (8.9 cm) diameter specimens were prepared by coring raw core using a saturated brine for cooling and flushing. Most recently, cores were turned using a tungsten carbide braze tool, Carboloy **AX-8**, type 883. Quality samples were machined with sharp edges **and** minimal chipping or shattering.

#### Apparatus and Experimental Procedures

##### Strength/Deformation Experiments

Tests were carried out in two existing triaxial apparatus which were described in an earlier report (2). These machines are suitable for **quasi-static** and creep experiments both in triaxial compression ( $\sigma_2 = \sigma_3$ ) and in triaxial extension ( $\sigma_2 = a, \sigma_3 = 0$ ). Stresses are generated by means of hydraulic fluid (silicon fluid) and by means of a cylindrical ram which acts parallel

## Experimental Results

### Quasi-Static Tests

The quasi-static tests results are summarized in Figures 3 through 12 and in Tables III and IV. The stair-step curves in Figures 3 and 16 are due to the special loading procedure which was followed in all experiments. Approximately constant mean loading rates were approached by successions of rapid load (stress) changes followed by periods during which the load (stress) was held constant. The mean loading rates which were obtained in this manner varied between  $1 \leq \frac{d}{dt}(\sigma_1 - a, ) \leq 2$  psi/s (7-14 kPa/s). The smooth traces in most of the figures are simply fits through the end points of each load-hold increment in the corresponding stair-step records. Tables III and IV list the maximum (ultimate) stresses and strains, the secant **moduli** and the quasi-static elastic constants.

All of the quasi-static data obtained fall into the normal ranges of rock salt properties. For example, the majority of published uniaxial compressive strengths lie between 2800 (19.3 MPa) and 3900 psi (26.9 MPa). The Bryan Mound data in Figures 3 through 6 and in Table III fall between the middle and upper end of that range. They are approximately 10-25% higher than the **uniaxial** compressive strengths of selected core **from** the Gulf Coast domes at **Tatum**, Bayou Choctaw, Jefferson Island and **Hockley** (6-9). However, the present uniaxial strength measurements are almost identical to results for West Hackberry salt and for rock salt from the bedded Wellington and **Salado** formations(2,10-12).

The same trends hold for the ultimate stresses in triaxial compression tests and for the ultimate strains which corresponds to the peak stress values  $(\sigma_1 - \sigma_3)_u$  in Table III. It is noted that table entries ">" and "<" indicate that the maximum stresses in several experiments lay below the ultimate stresses or that the strain data are either upper or lower bound estimates.

Table III

Maximum Stresses and Strains in Quasi-Static Tests,  
Subscripts u Pertain to Ultimate Stress and Strain  
Values.  $(e)_{um}$  is Volumetric Strain Calculated From  
Final Specimen Dimensions.

Test I.D.	$(\sigma_1 - \sigma_3)_u$ ( p s i )	$(e_1)_u$ (%)	$(-e_3)_u$ (%)	$(\gamma)_u$ (%)	$(e)_u$ (%)	$(e)_{um}^*$ (%)
Q/107A-3463/0/22	3770	2.15	2.68	4.83	-3.22	- 5.85
Q/107A-3967.5/0/60	3500	4.30	6.20	10.40	-8.00	-10.66
Q/107A-3964/2.0/22	11,000	$\geq 31.3$	$\geq 16.4$	$\geq 47.8$	$\leq -1.6$	- 4.5
Q/109A-2346/0/22	3780	2.85	3.16	6.00	-3.46	- 7.2
Q/109A-2348.5/0/60	3530	4.74	5.59	10.23	-6.43	-13.4
Q/109A-2347/2.0/22	9,900	$\geq 29.6$	$> 13.7^+$	$> 43.2^+$	$< -1.1^+$	-2.28
Q/109A-2350/2.0/60	$\approx 8070$	735.2	716.8	750.0	$< - .36$	-3.2
QE/109A-2351/2.0/22	$\approx 7250$	$\approx 5.10$	$\approx 8.73$	$\approx 13.83$	$< 1.48$	-----
Q/108B-3332/0/22	3280	1.80	4.20	6.0	-6.60	-8.85
Q/108B-3316.5/0.5/22	7250	$\approx 13.1$ $> 13.1$	$\approx 7.8^o$ $\approx 8.5^+$	$\approx 20.9^o$ $> 21.7^+$	$< -2.40$ $< -3.9^+$	$< -4.7^+$ $< -4.7^+$
QE1/108B-3326/2.0/22	74800	$\approx .96$	$< 1.9$	$\approx 2.9$	$< 0.02$	-----
QE2/108B-3326/0.5/22	7250	3.49	9.18	12.75 <sup>*</sup>	-2.20 <sup>*</sup>	-----
Q/107C-2509/0/60	3760	5.7	6.3	12.0	-7.0	

<sup>\*</sup> $(e)_{um}$  value determined from sample dimensions in more advanced state of failure.

<sup>+</sup> $(e_3)$ ,  $\gamma$  and  $e$  abnormally low because of possible dilatometer leak.

<sup>o</sup>Data based on dilatometric measurements

<sup>+</sup>Data based on disk gauge measurements.

<sup>\*</sup>Sum of strains accumulated during two successive extension experiments.

Table I

Summary of Ultrasonic Velocity Measurements Prior to Laboratory Testing

Sample I.D. (Drillhole #-Depth, ft.)	P-Wave Velocity ( $10^3$ ft/s)			S-Wave Velocity ( $10^3$ ft/s)		
	<u>Direction</u>			<u>Direction</u>		
	<u>Axial</u>	<u>Lateral 1</u>	<u>Lateral 2</u>	<u>Axial</u>	<u>Lateral 1</u>	<u>Lateral 2</u>
107A-3965	14.14	-----	-----	----	----	----
109A-2351	14.21	-----	-----	----	----	----
108B-3316.5	14.91	15.01	15.01	8.03	8.03	<b>8.13</b>
108B-3324	14.27	15.39	15.39	8.29	8.38	<b>8.13</b>
108B-3325	16.26	15.68	<b>16.06</b>	8.38	<b>9.18</b>	8.93
108B-3326	14.37	14.56	15.33	8.10	8.61	8.74
108B-3331	14.66	14.63	13.95	8.54	8.67	8.67
108B-3332	15.71	16.90	<b>16.90</b>	<b>7.90</b>	8.58	8.80
107C-2504.5	<b>12.96</b>	14.21	14.94	7.65	9.31	9.02
107C-2506	14.37	15.68	15.68	8.29	8.13	8.35
107C-2507	15.14	15.71	15.71	8.38	8.48	8.61
107C-2509	14.72	15.74	15.74	8.42	8.61	9.34
107C-2512	<b>13.60</b>	13.82	<b>14.18</b>	7.39	6.69	6.91
107C-2516	13.86	15.33	14.53	7.78	8.45	<b>8.32</b>

to the specimen axes. Fluid pressure and ram load are regulated by means of an incrementally servo-controlled pressure intensifier and a combination of a pump and large gas-filled accumulators.

Prior to testing all samples were coated with RTV **silastic** and enclosed in a flexible elastomer jacket between two stainless steel end-caps. The jackets isolated the specimens from the surrounding pressure fluid with negligible restraint on specimen deformation. It was also easy to penetrate the soft jackets to accommodate special fixtures to monitor sample deformation, acoustic emission or ultrasonic velocity.

Ram force was monitored by means of a load cell external to the pressure vessel. Fluid pressure was monitored with standard transducers. Axial salt deformation was determined with the aid of two diametrically opposed **LVDT's** (Linear Variable Differential Transformers) after suitable calibrations to account for system deformations within the active gauge length (3). Lateral deformation was determined by means of one or two disk gauges or it was measured dilatometrically (3,4). If the fluid pressure in the vessel remained constant, both techniques were used simultaneously.

#### Acoustic Emission Measurements

Acoustic emissions (AE) were detected and counted in a standard way (5). The piezoelectric transducers used were 0.5 in (13 mm) diameter disks of PZT-5 with a resonant frequency of **.5 MHz**. To ensure good acoustic contact with the sample, a special transducer holder was machined which rested directly on the salt but allowed the signal cable to pass through the rubber jacket surrounding the sample. The resultant signal was amplified 1000 times by an **Acoustic Emission Tech.** amplifier with a bandwidth of **.125-2 MHz**. The output noise level was approximately 50 **mV**. Acoustic emission events generated single amplitudes of 100 **mV** to several volts. The detection of the real

signal in the presence of noise was done in two stages. First, a variable threshold comparator was used to determine when the signal crossed some preset level that lay above the general noise, Then a counter was triggered by each successive level crossing in the signal. Only if 10 **crossings** occurred within 20  $\mu$ s was the event considered real. Following the detection of an event, the detector was turned off for 1 ms to avoid generating another count from the sometimes lengthy **AE** signal. At the observed count rates of less than 10 or 20 per second, the 1 ms dead time did not distort the count rates. After detection, the count was recorded on a counter for total acoustic emission and on a multichannel scalar for time resolved **AE** activity.

#### Data Reduction

All data reductions were performed on a PDP **11/34** computer. Details of this procedure are documented in a separate report (3). Therefore, only a few comments are necessary to aid the evaluation of the present results. Because stresses and strains were calculated from indirect measurements, care was **taken** in eliminating extraneous effects in the determination of the average axial stress and in the calculation of specimen strains. Axial stress calculations from measurements of the ram load P (Fig. 2) must consider at least two phenomena. If the rock undergoes large deformations, it changes substantially in cross-sectional area from its undeformed value **A0** to **AR** while the area of the loading ram **AP** remains **essentially** fixed. In addition, a zero shift of the load cell that measures P may occur during the heating phase in experiments at elevated temperature. Both of these effects, change in sample area and thermally induced zero shift of the load cell, were accounted for in the expression for the true axial stress

$$\sigma = CP + [(P - PR) - (CP - SR) \cdot AP] / AR \quad (1)$$

CP denotes the radial pressure during deviatoric loading. PR is the reaction of the warm load cell to the initial hydrostatic pressure SR.

Axial strain calculations are straightforward in principle. The main step is the elimination of the displacement contributions of several steel parts within the active gauge length. Inspection of Figure 2 reveals that for compression

$$\epsilon_x = \frac{1}{L_0} (\delta - \delta_v - \delta_{pL}) \quad (2)$$

For extension

$$\epsilon_x = \frac{1}{L_0} (\delta + \delta_v + \delta_{pL}) \quad (3)$$

$\epsilon_x$  denotes engineering (axial) strain.  $L_0$  is the undeformed specimen length. The remaining quantities are

$\delta$ : total displacement between gauge points A and B during deviatoric loading (Fig. 2).

$\delta_v$ : change in length of the pressure vessel, i.e., shift in the location of reference point B due to a pressure change (CP-SR).

$\delta_{pL}$ : change in length of the loading piston and end-caps, i.e., shift in location of reference point A due to changes of the ram force (P-PR) and confining pressure (CP-SR).

$\delta_v$  and  $\delta_{pL}$  are determined by calibrations and checked theoretically.

Because of the magnitude of the strains, engineering strains were later converted to natural strains according to the equations

$$e_1 = -\ln(1 + |\epsilon_1|) \quad (4)$$

$$e_3 = -\ln(1 + |\epsilon_3|) \quad (5)$$

$$\gamma = e_1 - e_3 \quad (6)$$

$$e = e_1 + e_2 + e_3 \quad (7)$$

$\gamma$  and  $e$  are shear strains and volumetric strains, respectively. Finally, the secant **moduli** and the elastic constants of rock salt under deviatoric loading were computed as follows. For triaxial compression at constant confining pressure,  $\sigma_3$

$$E = \frac{\Delta\sigma_1}{\Delta e_1} \quad (8)$$

$$\nu = \frac{|\Delta e_3|}{\Delta e_1} \quad (9)$$

For triaxial extension at constant **axial** stress,  $\sigma_1$

$$E = \frac{\Delta\sigma_1}{\Delta e_1 + \frac{1}{2}(\Delta e_3)} \quad (10)$$

$$\nu = \frac{\Delta e_3}{2\Delta e_1 + \Delta e_3} \quad (11)$$

The symbol  $\Delta$  denotes corresponding finite stress and strain increments.

#### Test Matrix

The experimental conditions for the eighteen tests of this report are listed in Table II. The test I.D. in the first column of Table II identifies all pertinent experimental parameters in the following format: nominal specimen diameter (in.), **type** of test (Q, **QE**, C or CE) and test stage/drillhole number-depth of core (**ft**)/**confining** pressure,  $\sigma_3$  (**ksi**)/test



Table II

Test Matrix

<u>Test I.D.</u>	<u>Test Description</u>
4Q/107A-3463/0/22	Unconfined quasi-static compression, $T = 22^{\circ}\text{C}$
3.5Q/107A-3967.5/0/60	Unconfined quasi-static compression, $T = 60^{\circ}\text{C}$
4Q/107A-3964/2.0/22	Quasi-static triaxial compression, $\sigma_3 = 2000 \text{ psi}$ , $T = 22^{\circ}\text{C}$
3.5C1/107A-3966/2.0/60	Triaxial compression creep, $\sigma_3 = 2020 \text{ Psi}$ , $(\sigma_1 - \sigma_3) = 1470 \text{ Psi}$ , $T = 60^{\circ}\text{C}$
3.5C2/107A-3966/2.0/60	Triaxial compression creep, $\sigma_3 = 2000 \text{ psi}$ , $(\sigma_1 - a_c) = 3135 \text{ psi}$ , $T = 60^{\circ}\text{C}$
3.5CE/107A-3965/2.0/60	Triaxial extension creep, $\sigma_3 = 2000 \text{ psi}$ , $(\sigma_1 - a_c) = 3020 \text{ psi}$ , $T = 60^{\circ}\text{C}$
4Q/109A-2346/0/22	Unconfined quasi-static compression, $T = 22^{\circ}\text{C}$
4Q/109A-2348.5/0/60	Unconfined quasi-static compression, $T = 60^{\circ}\text{C}$
4Q/109A-2347/2.0/22	Quasi-static triaxial compression, $\sigma_3 = 2000 \text{ psi}$ , $T = 22^{\circ}\text{C}$
3.5Q/109A-2350/2.0/60	Quasi-static triaxial compression, $\sigma_3 = 2000 \text{ psi}$ , $T = 60^{\circ}\text{C}$
3.5QE/109A-2351/2.0/22	Quasi-static triaxial extension, $\sigma_3 = 2000 \text{ psi}$ , $T = 22^{\circ}\text{C}$
4Q/108B-3332/0/22	Unconfined quasi-static compression, $T = 22^{\circ}\text{C}$
3.5Q/108B-3316.5/0.5/22	Quasi-static triaxial compression, $\sigma_3 = 500 \text{ psi}$ , $T = 22^{\circ}\text{C}$
3.5QE1/108B-3326/2.0/22	Quasi-static triaxial extension, $\sigma_3 = 2000 \text{ psi}$ , $T = 22^{\circ}\text{C}$
3.5QE2/108B-3326/0.5/22	Quasi-static triaxial extension, $\sigma_3 = 500 \text{ psi}$ , $T = 22^{\circ}\text{C}$
4Q/107C-2509/0/60	Unconfined quasi-static test, $T = 60^{\circ}\text{C}$
Q/107C-2504/2.0/22	Quasi-static triaxial compression, $\sigma_3 = 2000 \text{ psi}$ , $T = 22^{\circ}\text{C}$
4C/107C-2507/2.0/22	Triaxial compression creep, $\sigma_3 = 1990 \text{ psi}$ , $(\sigma_1 - \sigma_3) = 2990 \text{ psi}$ , $T = 22^{\circ}\text{C}$
3.5CE/107C-2504.5/2.0/22	Triaxial extension creep, $\sigma_3 = 2000 \text{ psi}$ , $(\sigma_1 - \sigma_3) = 2990 \text{ Psi}$ , $T = 22^{\circ}\text{C}$

temperature ( $^{\circ}\text{C}$ ). Q and QE denote quasi-static triaxial compression and extension tests, respectively. C and CE refer to creep tests in triaxial compression and extension. Successive test stage numbers are used if more than one experiment was performed on a given sample. Thus, the code **3.5QE2/108B-3326/0.5/22** means: nominal sample diameter 3.5 in., quasi-static extension experiment, second test following an earlier experiment on the same sample/drillhole **108B-core** depth 3326 ft./confining pressure  $\sigma_3 = 0.5 \text{ ksi/test}$  temperature **22 $^{\circ}\text{C}$** . For simplicity, the nominal specimen diameter will be omitted in all subsequent tables.

The choice of experimental conditions in Table II was motivated by four considerations. (1) Obtain data which can be compared directly with published results for rock salt from other locations, (2) Establish the variability of the mechanical properties of Bryan Mound core from different parts of the dome, (3) Evaluate the influence of temperature and confining pressure on the strength, ductility and creep properties of Bryan Mound material, and (4) Ascertain differences in rock salt response between triaxial compression and triaxial extension.

Limited core footage and limited time made it impossible to devise an all-encompassing test matrix. Therefore, the list in Table II constitutes a compromise by which, for example, the uniaxial compressive strength at **22 $^{\circ}\text{C}$**  was compared in spot checks on samples from drillholes **107A**, **108B** and **109A**. In turn, the unconfined rock salt response at **60 $^{\circ}\text{C}$**  was measured on selected specimens from drillholes **107A**, **107C** and **109A** but not **108B**. The duration of creep experiments was determined primarily by a combination of **SPR** schedules and by the availability of test facilities during the period of this study.

the abnormal response of Bryan Mound core is due to the unusual nature of the impurity distribution, Apparently, almost all of the anhydrite is contained as disseminated intracrystalline as opposed to intercrystalline impurities. Further experimental work is suggested to resolve some of these questions. In the meantime, it appears that the use of constitutive data for rock salt from other locations is likely to overpredict the time-dependent deformation in salt at Bryan Mound.

The results in Table VIII were obtained by fits to the axial specimen strains  $e_x$ , which are always largest and, therefore, least susceptible to experimental errors. These axial strains can be converted readily to shear strains using

$$\gamma = e_1 - e_3 \approx 3/2 |e_x| \quad (15)$$

with  $e_2 = e_3$  in compression and  $e_2 = e_1$  in extension provided

$$e = e_1 + e_2 + e_3 \approx 0$$

This latter condition is approximately satisfied in most creep experiments on rock salt in the sense that the shear strains are very much larger than the volumetric strains. However, this does not imply that the volumetric strains are exactly zero. Although difficult to resolve, comparatively small volume changes are important to assess the creep fracture potential of rock salt. Fast experiments suggested that the volumetric strains are considerably smaller in triaxial extension than they are in triaxial compression. This same trend is suggested by the data in Fig. 15. At the same time, physical observations provide direct evidence that very small (negative) volume changes during creep may be caused by large numbers of microcracks as possible

Table IV

Summary of Secant Moduli of Bryan Mound Salt Upon First Laboratory  
Loading and List of Elastic Constants

Test I.D.	Secant Mod. ( $10^5$ psi)/Princ. Strain Ratio $500 \leq (\sigma_1 - \sigma_3)(\text{psi}) \leq 2000$	Elastic (Unloading) Constants	
		$E(10^6 \text{ psi})/\nu$	
Q/107A-3463/0/22	4.34/0.90	---mm.---	
Q/107A-3967.5/0/60	2.03/0.94	-----	
Q/107A-3964/2.0/22	10.8/0.40	5.43/0.29	a. 10
Q/109A-2346/0/22	2.02/1.06	-----	
Q/109A-2348.5/0/60	1.47/1.07	-----	
Q/109A-2347/2.0/22	4.51/0.47	5.05/0.31	1.07
Q/109A-2350/2.0/60	3.2/0.42	5.0/0.36	1.838
QE/109A-2351/2.0/22	4.12/0.40	5.14/0.50	1.1
Q/108B-3332/0/22	2.72/1.30	-----	
Q/108B-3316.5/0.5/22	3.46/0.58	4.36/0.37	1.01
QE1/108B-3326/2.0/22	6.6/0.51	3.2/0.27	1.0
QE2/108B-3326/0.5/22 *	-----	3.4/0.32	1.28
Q/107C-2509/0/60	1.52/0.99	-----	

\*Test preceded by earlier laboratory history.

Table V

Average Dynamic Elastic Constants for Rock Salt From Drillholes  
**107A, 107C, 108B** and **109A** Based on Ultrasonic Velocity Data in  
 Table II and Density  $\rho = 2.17 \text{ gm/cc.}$

	Core Direction		
	<u>Axial</u>	<u>Lateral</u>	<u>Lateral</u>
Elastic Modulus E ( $10^6$ psi)	5.14	5.57	5.24
Poisson's Ratio	0.28	0.28	0.28
$\nu$			

Little difference is indicated in the response of salt from the four different drillholes although the core **109A** was purer, considerably more homogeneous and free from anhydritic bands which were common in the remaining holes. Greater ductility at higher temperature tends to obfuscate completely subtle differences in mechanical response due to variations in rock salt composition and texture (Figs. 4-6 and 12).

The effect of confining pressure at 500 psi (3.5 MPa) and 2000 psi (13.8 MPa) is consistent with published results. Similar data are available for **Salado** salt and for dome salt from **Hockley** and Weeks Island (9,10,13). The same conclusions apply to the secant moduli and to the quasi-static elastic constants in Table IV. The two low values of  $E \approx 3.3 \times 10^6$  psi (22.8 GPa) were measured on the same sample. The remaining values fall between the bounds  $4.36 \times 10^6 \leq E \leq 5.43 \times 10^6$  (30.1 to 37.4 GPa) psi and  $0.27 \leq \nu \leq 0.37$  (0.50). No satisfactory explanation can be offered for one exceptionally high value of Poisson's ratio,  $\nu = 0.50$  in test **QE/109A-2351/2.0/22**. Modulus measurements in **uniaxial** tests were omitted because they were limited to **post-peak** values which are lower than the intrinsic elastic constants. For comparison, the average dynamic elastic constants parallel to and perpendicular to the core axes are compiled in Table V based on an average rock salt density of 2.17 g/cc. Close agreement between the static and elastic dynamic elastic constants supports the assumption that laboratory experimental data can be used to evaluate the response of rock salt in situ,

Three quasi-static extension experiments were performed. The results at 2000 psi (13.8 MPa) confining pressure agree with earlier data for West Hackberry material. Samples from West Hackberry and Bryan Mound exhibited essentially the same shear response in compression and extension but showed systematic differences in volume strain behavior (e.g., **Figs. 10-12**). Although

fracture did not occur at 2000 psi (13.8 MPa) confining pressure, the differences in volumetric strains between compression and extension suggested that the ultimate stresses and failure modes might be different as well. Contrary to expectation, however, core from drillhole 108B had the same ultimate stress in compression and extension at 500 psi (3.5 MPa) confining pressure, and the volumetric strains appeared to be similar within the uncertainty of the measurements (Table III). Nevertheless, at least the shear strains to failure and the fracture modes differed markedly. Extension fracture occurred at approximately half the shear strain observed at failure for compression (Table III). Also, extension failure took place very suddenly along a single, sharply defined extension fracture parallel to the direction of greatest compression,  $\sigma_2 = \sigma_1$ . Triaxial compression failure was more gradual and stable. The difference in failure mode was related to a difference in the preferential alignment of microfractures which was evident both in quasi-static conditions and in creep (Fig. 13). Future experiments will pursue these fracture observations. Efforts will also be made to resolve the problem of obtaining representative radial deformation measurements which are critical for valid volumetric strain calculations. This problem is demonstrated by the comparison of data for test Q/108B-3316.5/0.5/2 in Table III. A 10 percent difference in radial strain  $e_3$  produced a discrepancy of more than 60 percent in the calculated volumetric strain. The differences in  $e_3$  are likely to be the result of shortcomings in measurement techniques. Disk gauge measurements were restricted to at most two diameters and, therefore, subject to local inhomogeneities in the strain field (14). On the other hand, strain data based on dilatometric measurements provide averages over the entire specimen length including the ends. Therefore, dilatometric measurements reflect the contribution of end restraints, particularly as macroscopic fracture ensues,

### Creep Experiments

The creep data obtained are shown in Tables VI and VII and in Figs. 14 and 15. The true stress was maintained constant in three of the five tests to within no more than  $\pm 50$  psi (0.3 MPa). However, difficulties were encountered in the stress control during the remaining two experiments. Beginning at the 140th hour of test C/107C-2507/2.0/22 the average principal stress difference dropped by 35 psi (0.2 MPa). In the same test, excursions of plus or minus 100 psi (0.7 MPa) occurred in  $(\sigma_1 - \sigma_3)$  during the 180th, 235th and 245th hour of testing. An even more drastic stress variation was encountered in test CE/107A/2.0/60 between the 10th and 33rd hour of the experiment. The confining pressure dropped by 380 psi (2.6 MPa) resulting in an almost equal increase in the principal stress difference and in a very distorted record of primary creep strain versus time (Fig. 14). Finally, it is noted that the initial strain of test C2/107A-3966/2.0/60 was influenced by creep during an earlier test at a lower principal stress difference (Tables II and VI) and that doubtful radial strain measurements were collected in that experiment.

A cursory interpretation of the present creep results was based on several assumptions which were invoked and tested in other studies on rock salt creep (15-17). First, it was assumed that salt creep was due to primary, transient creep,  $e_p$  as well as secondary creep  $\dot{e}_{xs}$  which fit the relationship

$$e_x = e_{x0} + \frac{e_p}{x_p} + \dot{e}_{xs} t \quad (12)$$

and

$$e_{xp} = e_{xa} (1 - \exp(-\xi t)) \quad (13)$$



Table VI

Summary of Data From Creep Experiments. Quantity  $\dot{\epsilon}_x$  was Determined From Linear Least Square Fits to Experimental Data Over the Last 40 to 50 Hours of Each Experiment.

Test I.D.	$(\sigma_1 - \sigma_3)$ (psi)	$\sigma_3$ (psi)	Initial loading Rate (psi/s)	Test Duration (hrs)	Initial Strains $e_1$ (%) - $e_3$	Min. Observed Axial Creep Rate $\dot{\epsilon}_x$ ( $10^{-9}$ 1/s)
C1/107A-3966/2.0/60	1470	2020	130	410	.17 .034	0.252
C2/107A-3966/2.0/60	3135	2000	120	332	.33 .093	2.20
CE/107A-3965/2.0/60	3020	2000	25	457	.37 .78	0.91
C/107C-2507/2.0/22	2990	1990	75	280	.25 .12	2.75
CE/107C-2504.4/2.0/22	2990	2000	26	264	.16 .39	1.24

Table VII

Fitting Parameters for Axial Creep Strains,  $e_x$

$$e_x = e_{x0} + e_{xa}(1 - \exp(-\xi t)) + \dot{e}_{xs} t$$

(time t in seconds)

<u>Test I.D.</u>	<u>Parameter Values</u>			
	<u><math>e_{x0}</math></u>	<u><math>e_{xa}</math></u>	<u><math>\xi</math></u>	<u><math>\dot{e}_{xs}</math></u>
C1/107A-3966/2.0/60	9.44E-4	1.57E-3	5.46E-3	3.63E-10
C2/107A-3966/2.0/60	1.79E-3	2.82E-3	6.12E-6	2.02E-9
CE/107A-3965/2.0/60	1.38E-3	5.38E-3	1.79E-3	2.26E-9
C/107C-2507/2.0/22	5.60E-3	3.46E-3	9.86E-6	3.82E-9
CE/107C-2504.5/2.0/22	2.68E-3	1.98E-3	1.19E-5	1.97E-9

Furthermore, secondary creep was described by an equation for diffusion controlled creep (18),

$$\dot{\epsilon}_{xs} = A \exp(-Q/RT) \left( \frac{\sigma_1 - \sigma_3}{\mu} \right)^n \quad (14)$$

The parameters  $\epsilon_{xo}$ ,  $\epsilon_{xa}$ ,  $\xi$  and  $\dot{\epsilon}_{xs}$  were obtained for the largest linear (axial) creep strains by means of nonlinear least square fits and are summarized in Table VII. It is emphasized that these data have not been corrected for likely effects of strain and loading histories including differences in initial loading rates (Table VI). The stress exponent  $n$  in Equation (14) was determined to be 2.27 from the secondary creep rates of the two-stage experiment at 60°C in Tables VII and VIII. Within the data scatter no temperature effect was observed so the activation energy  $Q$  remains unknown.

A comparison of the present data with published results creates several difficulties. Most strikingly, the available secondary creep rates for Bryan Mound core are one to two orders of magnitude smaller than typical secondary creep rates for rock salt reported elsewhere. In addition, no temperature effect was evident within the considerable scatter of the data at 22 and 60°C, and the stress exponent  $n = 2.27$  compares with a **typical value** of  $n \approx 5$  (17). The discrepancy in  $n$  might be due to the fact that steady state creep was not actually attained in one or both experiments. However, to raise  $n$  from 2.27 to 5 would require a large, significant increase in the ratio of the creep rates ( $\dot{\epsilon}_{xs}$ ) for the first two creep tests in Tables VI and VII.

Although it is dangerous to generalize the small number of results of this study, the combination of observations suggests that Bryan Mound salt might be less prone to creep than, for example, rock salt from the West Hackberry dome. No satisfactory explanation can yet be offered for this behavior. However, unpublished petrographic data (1) raise the possibility that

precursors to time dependent fracture unless microfracturing is balanced by subsequent crack healing, Examples of a microfracture network i triaxial extension at  $\sigma_3 = 2000$  psi and  $60^\circ\text{C}$  are shown in Fig. 13.

#### Acoustic Emissions

Acoustic emissions were monitored in one test, Q/108B-3316.5/0.5/22. **These** results are shown in Figs. 16 and Figs. 17 and demonstrate direct correlations between acoustic emissions and inelastic deformation of rock salt. Specifically, Fig. 17 shows a one-to-one correspondence between acoustic emissions and volumetric strain. This correspondence indicates that acoustic emissions are due to microfracturing, i.e., void formation or, alternatively, that microfracturing is common in rock salt at low confining pressure and temperature. Microfracturing and acoustic emissions occur at relatively low principal stress difference and are surprisingly pronounced during stress reversals. The AE activity during unloading (Fig. 16) is attributed to the effect of inhomogeneous inelastic deformations. This view is consistent with the observation that the number of AE events during unloading appeared to increase with increasing inelastic strain. Little or no acoustic emission activity was recorded during reloading until close to the point of maximum stress which had been reached previously. Based on the quality of the acoustic emission measurements during this study, it is planned to utilize these measurements routinely to monitor damage accumulation under a wide variety of experimental conditions.

#### Summary and Conclusions

Fourteen quasi-static experiments and five creep tests were described together with the results of ultrasonic velocity and acoustic emission measurements. The quasi-static behavior of Bryan Mound salt was normal compared with published material properties for rock salt from other locations, including

dome salt and bedded salt. Noticeable differences in texture and the presence of **anhydrite** rich bands had no major influence on the unconfined and **triaxial** compressive strength, the ultimate strains, the secant moduli during first laboratory loading and the elastic constants. Temperature change from 22 to 60°C resulted in increased ductility and in an approximately 25% drop in the peak stress. No significant differences were observed between results from four different drillholes.

Contrary to the consistency of all quasi-static data, creep of Bryan Mound salt was anomalous. Based on the smallest observed creep rates and based on data fits to a combined primary/secondary creep model, creep was one to two orders of magnitude slower than the creep of rock salt reported elsewhere. No temperature effects were evident within the scatter of available data at 22 and 60°C. Finally, the observed stress dependency of secondary creep was given by a stress exponent of  $n = 2.27$  which is considerably smaller than the normal value of  $n \approx 5$  for data gathered under similar experimental conditions and fit to the same equations,

Comparative results in **triaxial** compression and extension are not totally conclusive. However, in spite of limited results it appeared that the change of the intermediate principal stress from the condition  $\sigma_2 = \sigma_3$  to  $\sigma_2 = \sigma_1$  led to a change in the geometry of induced microfracture networks. As a result, the rock salt became more brittle, fracture occurred at smaller strains in **extension** compared with the failure strains in compression and the fracture mode changed from multiple, conjugate fractures which were inclined to the direction of greatest compression,  $\sigma_1$  to a single extension fracture parallel to  $\sigma_1$ .

Acoustic emissions were monitored in one experiment with excellent results and direct correlations between AE activity, shear ~~strai~~ and volumetric strain. Volumetric strains were small in creep. Nevertheless, creep still led to the development of microfractures even in an extension experiment at 2000 psi (13.8 MPa) confining stress and 60°C temperature. Microfracturing may change the permeability of rock salt and may be a precursor to creep fracture.

### References

1. Bild, R. W., personal co-cation, Sandia National Laboratories, 1980.
2. Wawersik, W. R. and D. W. Hannum, "Mechanical Behavior of New Mexico Rock Salt in Triaxial Compression Up to 200°C," J. Geophys. Res., **85**, B2, 891-900, (1980).
3. Wawersik, W. R., "Indirect Deformation (Strain) Measurements and Calibrations in Sandia Triaxial Apparatus for Testing to 250°C," SAND79-0114, Sandia National Laboratories, (1979).
4. Schuler, K. W., "Lateral Deformation Gauge for Rock Mechanics Testing," Exp. Mech., **18**, 12, (1978).
5. Wu, F. T. and L. Thomsen, "Microfracturing and Deformation of Westerly Granite Under Creep Conditions," Int. J. Rock Mech. Min. Sci., **12**, (1975).
6. U. S. Corps of Engineers, "Project Dribble: Petrographic Examination and Physical Tests of Cores, Tatum Salt Dome, Mississippi," Tech. Rept. 6-614, Army Eng. Waterways Exp. Sta., Vicksburg, Mississippi, (1963).
7. PB/KBB, "Strategic Petroleum Reserve Program, Salt Dome Geology and Stability Analysis Bayou Choctaw, Louisiana," Techn. Report to U. S. Dept. of Energy, (1978).
8. Hansen, F. D., "Case History Rock Mechanics Examination of the Jefferson Island Mine: II. Laboratory Evaluation of Strength and Creep Deformation Characteristics of Dome Salt Under Confining Pressure," Techn. Memo. Rep. RSI-0057, (1978).
9. Thompson, E. and E. A. Ripperger, "An Experimental Technique for the Investigation of the Flow of Halite andylvinite," Proc. Sixth Symp. Rock Mech., Univ. of Missouri at Rolla, (1964).
10. Wawersik, W. R., D. W. Hannum and H. S. Lauson, "Compression and Extension Data for Dome Salt From West Hackberry, Louisiana," SAND79-0668, Sandia National Laboratories, (1980).
11. Hansen, F. D., "Quasi-Static and Creep Deformational Characteristics of Bedded Salt From the Carey Mine Near Lyons, Kansas," Techn. Memo. Rep. RSI-0067, RE/SPEC, Inc., Rapid City, SD, (1978).
12. Hansen, F. D. and P. F. Gnirk, "Design Aspects of the Alpha Repository: III. Unisxial Quasi-Static and Creep Properties of the Site Rock," Techn. Memo. Rep. RSI-0029, RE/SPEC, Inc., Rapid City, SD, (1975).
13. Hansen, F. D., "Quasi-Static Strength and Deformational Characteristics of Salt and Other Rock From the Weeks Island Mine," Techn. Memo. Rep. RSI-0061, RE/SPEC, Inc., Rapid City, SD, (1977).
14. Wawersik, W. R., J. F. Callender, R. Weaver and R. K. Dropek, "Preliminary Determination of Mechanical Properties of Rock Salt From Southeastern New Mexico," Pre-Proc. 17th U.S. Symp. Rock Mech., Univ. of Utah Experiment Station, Salt Lake City, UT, (1976).

15. Munson, D. E. and P. R. Dawson, "Constitutive Model for the Low Temperature Creep of Salt (With Application to WIPP)," SAND79-1853, Sandia National Laboratories, (1979).
16. Herrmann, W., W. R. Wawersik and H. S. Lauson, "Creep Curves and Fitting Parameters for Southeastern New Mexico Bedded Salt," SAND80-0087, Sandia National Laboratories, (1980).
17. Herrmann, W., W. R. Wawersik and H. S. Lauson, "Analysis of Steady State Creep of Southeastern New Mexico Salt," SAND80-0558, Sandia National Laboratories, (1980).
18. Weertman, J., "Dislocation Climb Theory of Steady State Creep," Trans. AIME, 61, (1968).





Banded Salt



Unbanded Salt

Figure 1: Rock Salt From Bryan Mound Dome With and Without Steeply Dipping Anhydrite Rich Bands Accentuated by Back-Illumination.

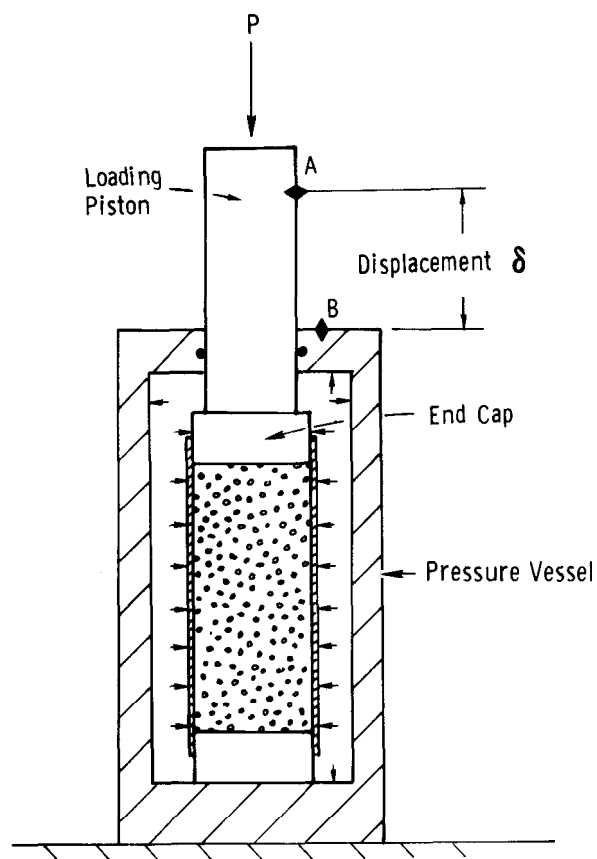


Figure 2: Schematic of Sandia Triaxial Apparatus Showing Reference Points A, B for Axial Displacement Measurement  $\delta$ .

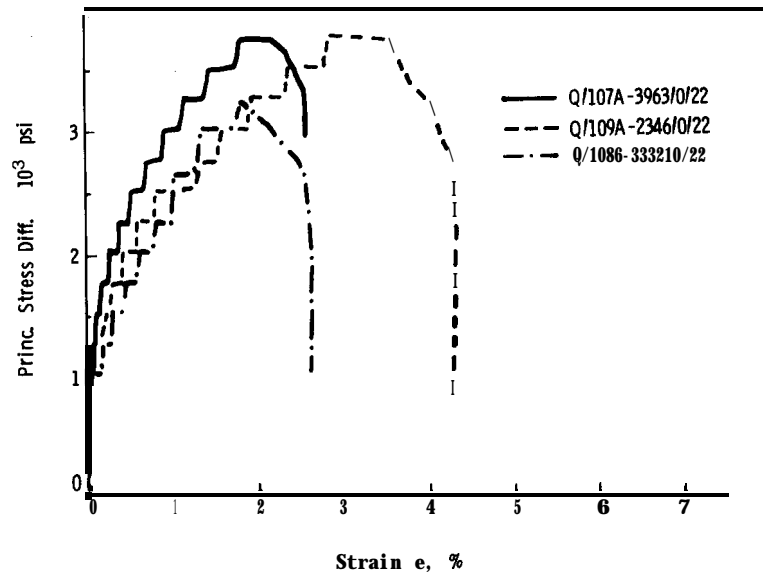


Figure 3: Quasi-Static Uniaxial Compression Data at 22°C. Core From Drillholes 107A, 109A and 108B.

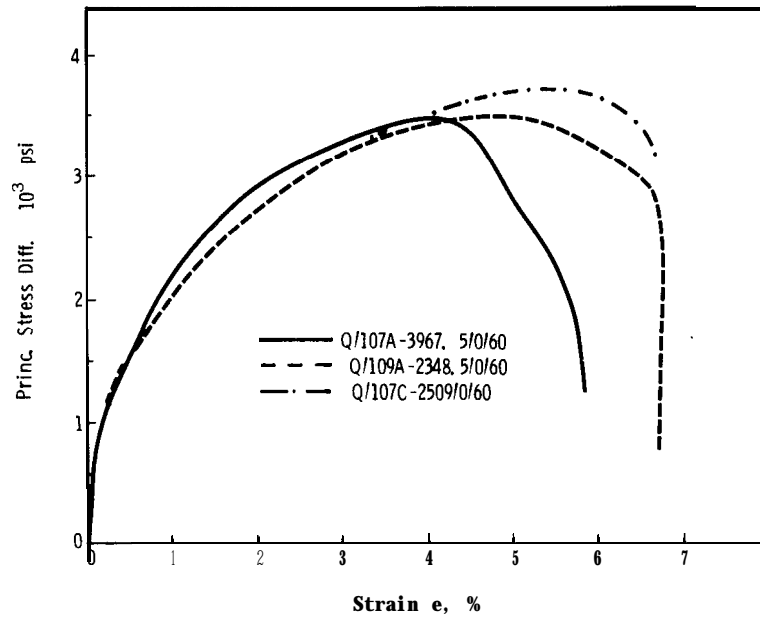


Figure 4: Quasi-Static Uniaxial Compression Data at 60°C,  $(\sigma_1 - \sigma_3)$  vs.  $e_1$ . Core From Drillholes 107A, 107C and 109A.

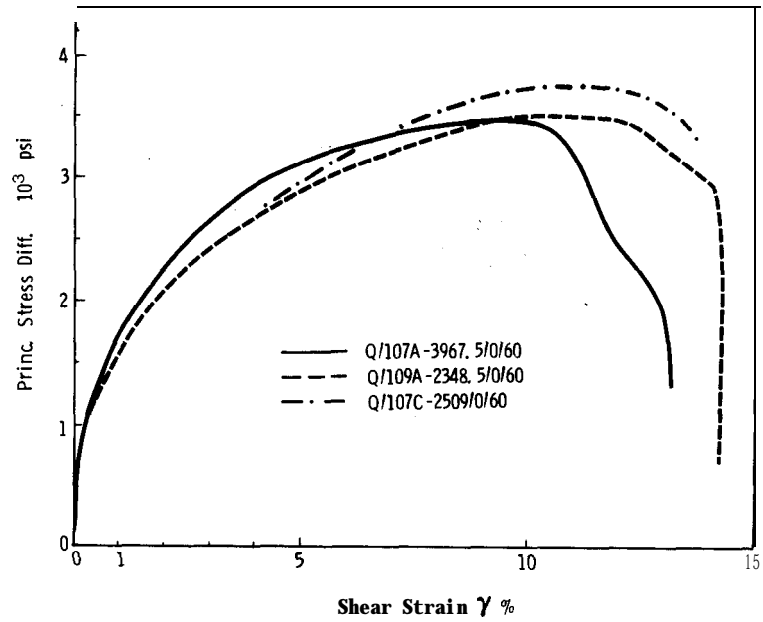


Figure 5: Quasi-Static Uniaxial compression Data at  $60^{\circ}\text{C}$ ,  $(\sigma_1 - \sigma_3)$  vs.  $\gamma$ . Core From Drillholes 107A, 107C and 109A -- Same Tests as Experiments in Figs. 4 and 6.

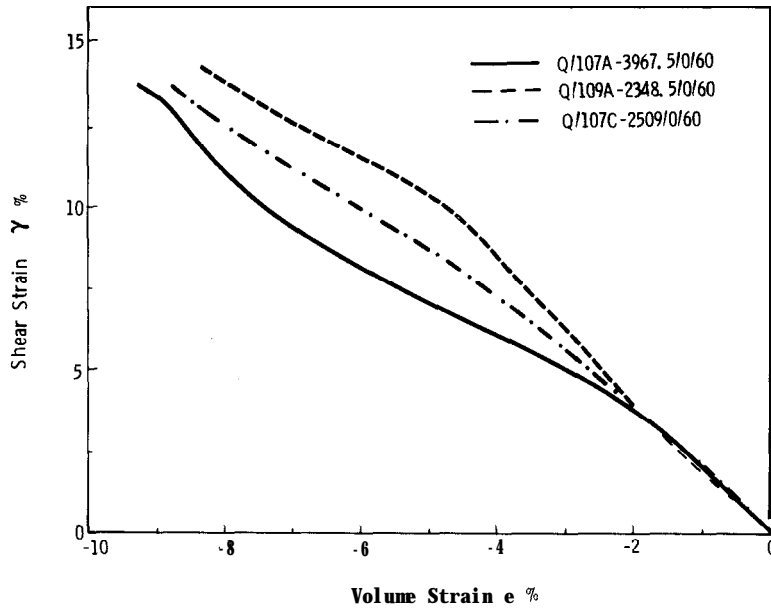


Figure 6: Quasi-Static Uniaxial Compression Data at  $60^{\circ}\text{C}$ ,  $\gamma$  vs.  $e$ . Core From Drillholes 107A, 107C and 109A -- Same Tests as Experiments in Figs. 4 and 5.

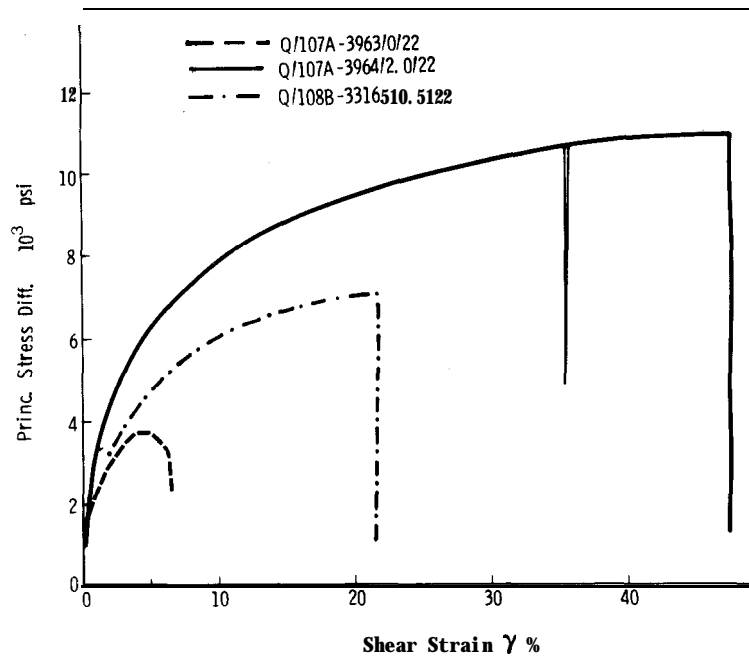


Figure 7: **Quasi-Static Triaxial Compression Data at 22°C,  $(\sigma_1 - \sigma_3)$  vs.  $\gamma$ .** Core From Drillholes 107A and 108B. Strain Data for Q/108B-3316.5/0.5/22 Averaged From Dilatometric and Disk Gauge Measurements.

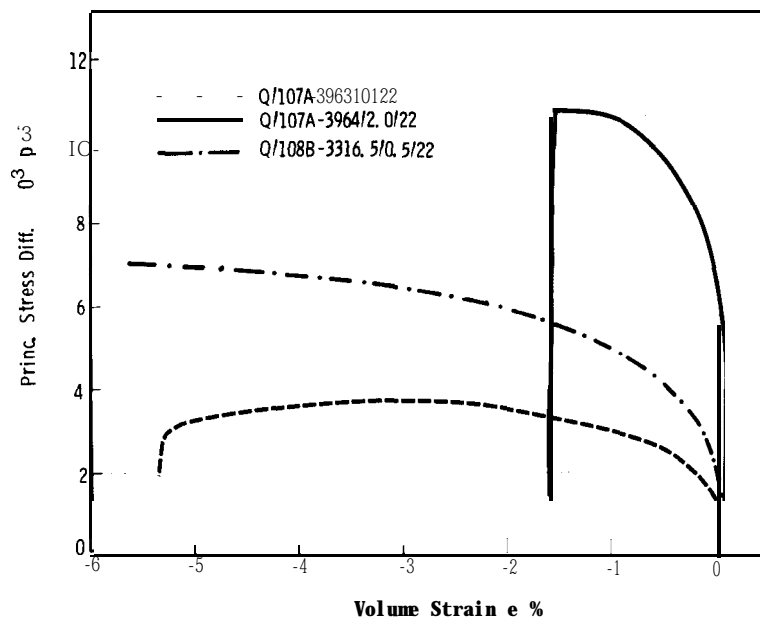


Figure 8: **Quasi-Static Triaxial Compression Data at 22°C,  $(\sigma_1 - \sigma_3)$  vs.  $e$ .** Core From Drillholes 107A and 108B. Strain Data for Q/108B-3316.5/0.5/22 Averaged From Dilatometric and Disk Gauge Measurements -- Same Tests as Experiments in Figs. 7 and 9.

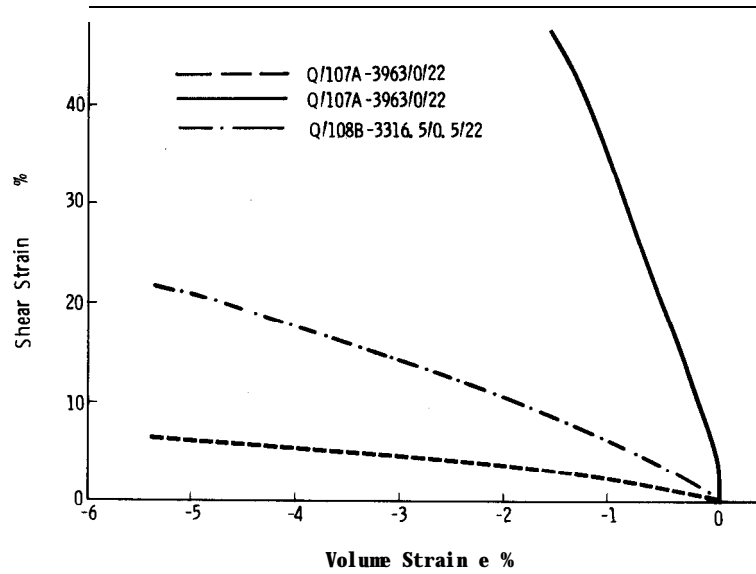


Figure 9: **Quasi-Static** Triaxial Compression Data at 22°C,  $\gamma$  vs.  $e$ . Core From Drillholes 107A and 108B. Strain Data for Q/108B-3316.5/0.2/22 Averaged From Dilatometric and Disk Gauge Measurements -- Same Tests as Experiments in Figs. 7 and 8.

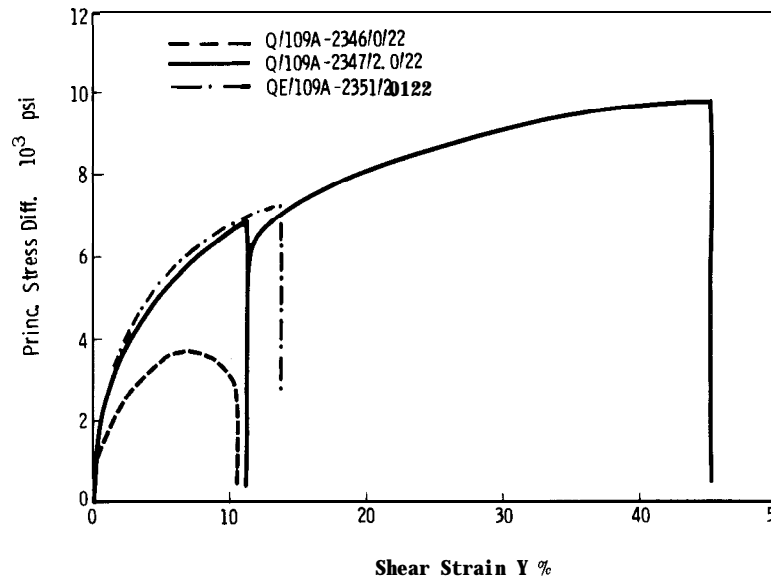


Figure 10: Quasi-Static Compression and Extension Data at 22°C,  $(\sigma_1 - \sigma_3)$  vs.  $\gamma$ . Core From Drillhole 109A.

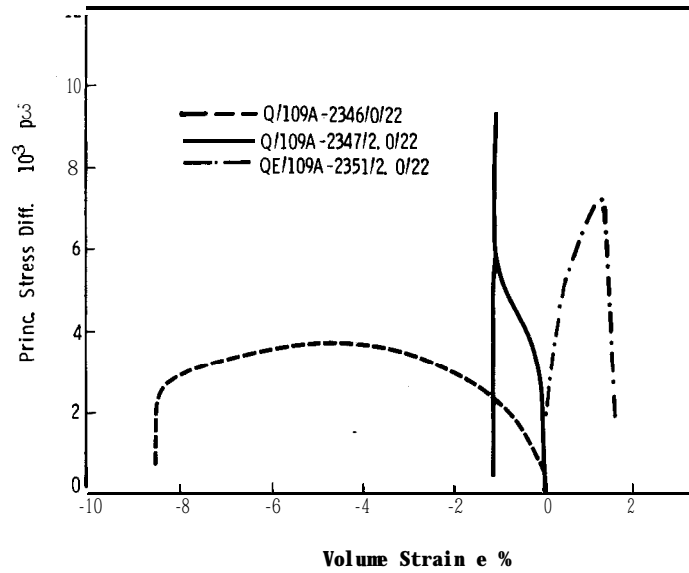


Figure 11: Quasi-Static Compression and Extension Data at 22°C,  $(\sigma_1 - \sigma_3)$  vs.  $e$ . Core From Drillhole 109A. Volumetric Strain Data at  $\sigma_3 = 2000$  psi Questionable. Same Tests as Experiments in Fig. 10.

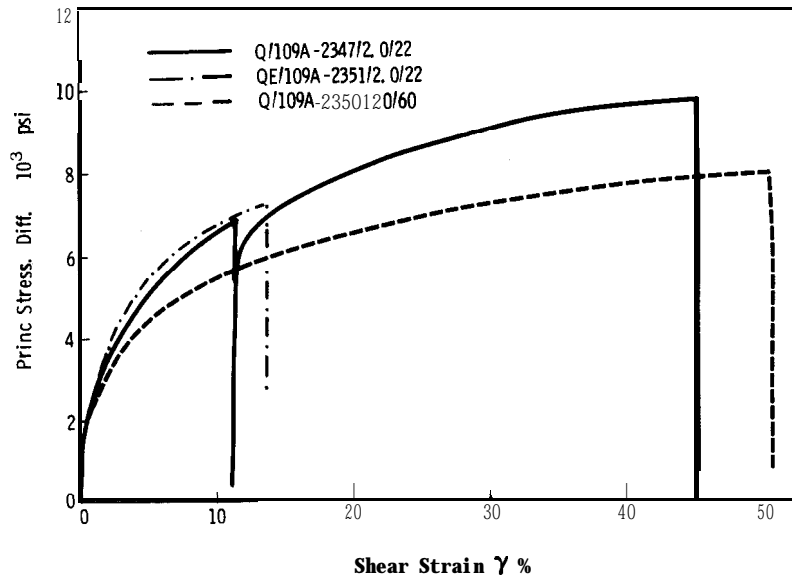


Figure 12: Quasi-Static Compression and Extension Data at 22 and 60°C. Core From Drillhole 109A.

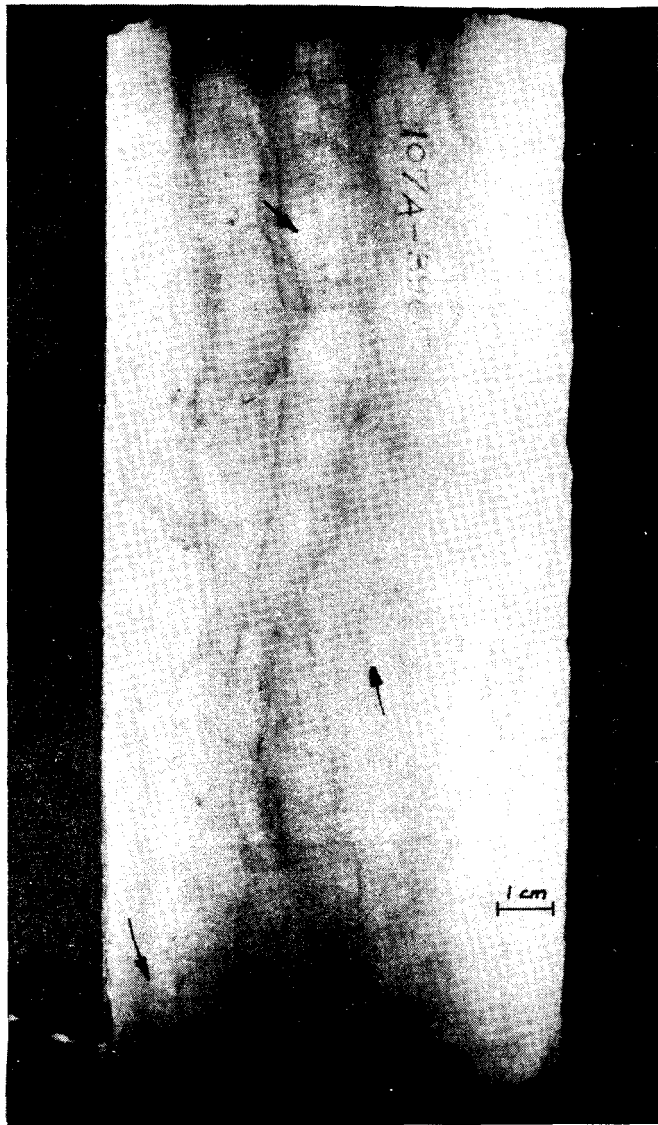


Figure 13: Deformed Specimen After Triaxial Extension Creep Experiment at  $\bar{\sigma} = 2000$  psi,  $(\sigma_1 - \sigma_2) = 3020$  psi and  $60^\circ\text{C}$  (Test CE/107A-3965/2.0/60). Note Abundance of Microcracks Normal to Cylinder Axis (Selected Arrows),



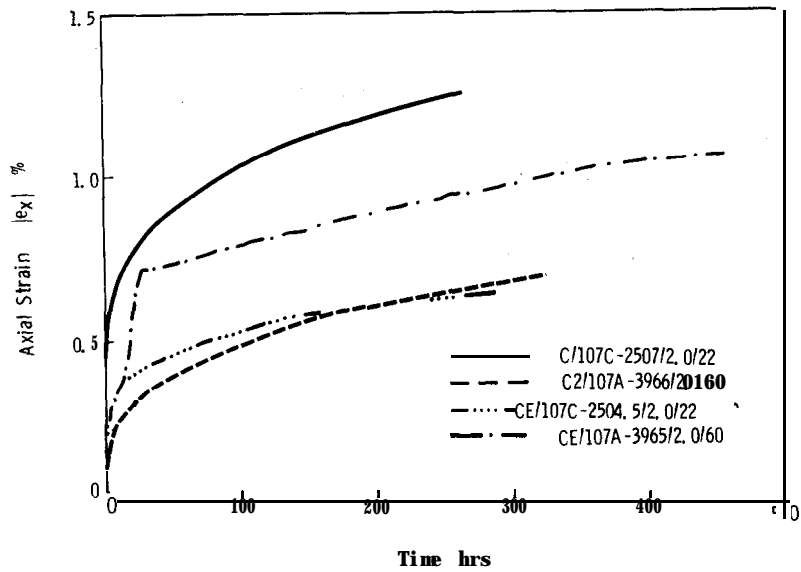


Figure 14: Creep Data in Triaxial Compression and Extension at  $(\sigma_1 - \sigma_3) \approx 3000$  psi and at 220C and 60°C.  $|e_x|$  vs. Time. Core From Drillholes 107A and 107C.

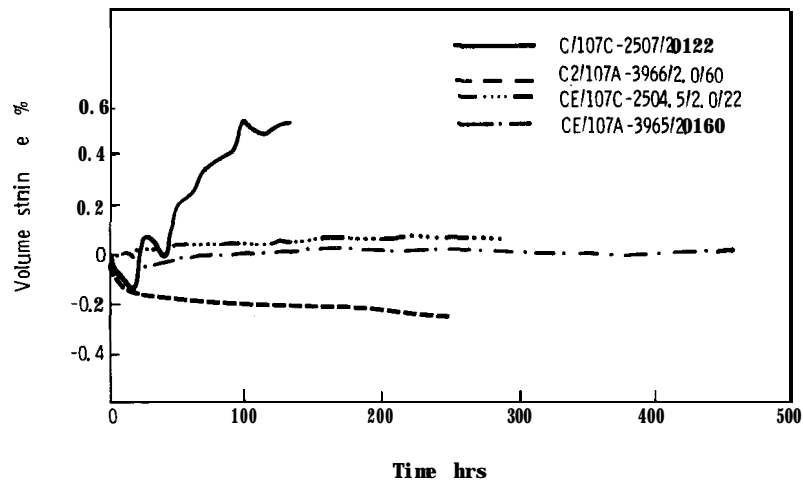


Figure 15: Creep Data in Triaxial Compression and Extension at  $(\sigma_1 - \sigma_3) \approx 3000$  psi and at 22 and 60°C,  $e$  vs. Time. Core From Drillholes 107A and 107C -- Same Tests as Experiments in Fig, 14.

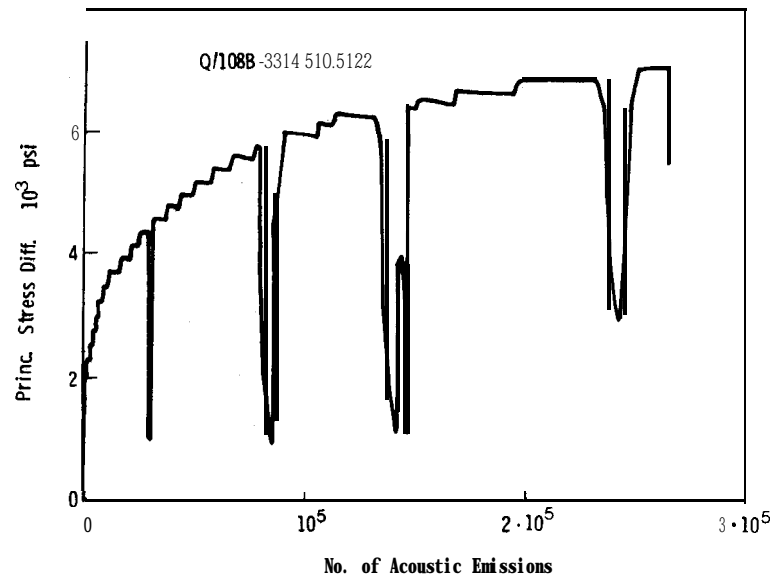


Figure 16: Principal Stress Difference vs. Acoustic Emissions in Triaxial Compression Test. Note Similarity of Record with Corresponding Curve  $(\sigma_1 - \sigma_3)$  vs.  $\gamma$  in Figure 7.

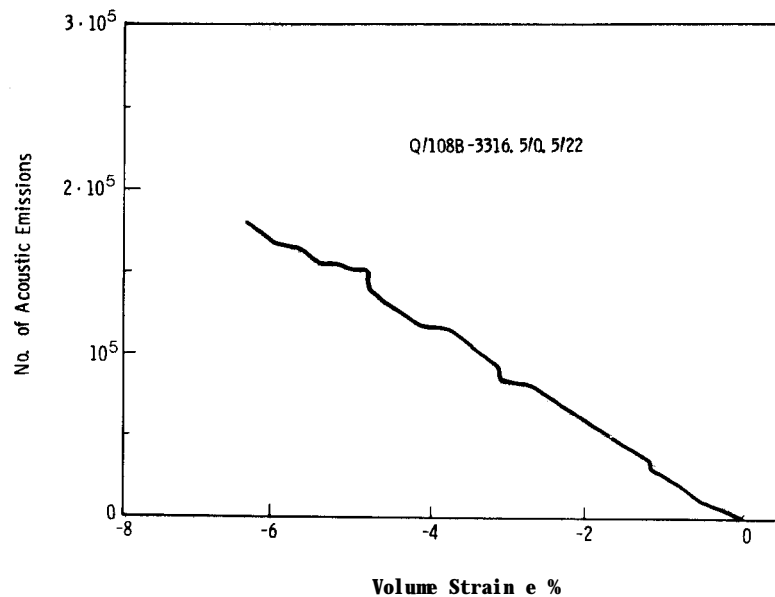


Figure 17: Acoustic **Emission** Activity vs. Volumetric Strain During Test of Figures 7 and 16. Radial Strain Data Based on Disk Gauge Measurements Only

Distribution: (Materials Report)

U. S. Department of Energy  
Strategic Petroleum Reserve  
Project Management Office

900 Commerce Road East  
New Orleans, LA 70123

Attn: C. C. Johnson  
R. W. Mazurkiewicz (5)  
G. J. Scango  
G. A. Stafford

U. S. Department of Energy  
Strategic Petroleum Reserve

1726 M Street NW  
Washington, DC 20461

Attn: Larry Pettis

Aerospace Corporation

800 Commerce Road East, Suite 310  
New Orleans, LA 70123

Attn: Elliott Katz

Parsons-Gilbane

800 Commerce Road West  
New Orleans, LA 70123

Attn: Wal-ter Marquardt

Dravo Utility Constructors, Inc.

850 S. Clearview Pkwy.  
New Orleans, LA 70123

Attn: C. Ashline

Jacobs/D'Appolonia Engineers (2)

6226 Jefferson Hwy., Suite B  
New Orleans, LA 70123

Attn: Harold Kubicek  
c/o Bill Walker

Aerospace Corporation

2350 East El Segundo Blvd.  
El Segundo, CA 90009

Attn: Guy F. Kuncir

R. L. Thoms

Louisiana State University  
Institute for Environmental Studies  
Atkinson Hall  
Baton Rouge, LA 70803

4000 A. Narath

4500 E. H. Beckner

4540 M. L. Kramm

4541 L. W. Scully

4543 J. F. Ney

4543 R. R. Beasley (5)

4543 M. H. Gubbels

4745 J. R. Tillerson

5000 J. K. Galt

5500 O. E. Jones

5510 D. B. Hayes

5511 J. W. Nunziato

5520 T. B. Lane

5522 T. G. Priddy

5522 S. E. Benzley

5522 D. S. Preece

5530 W. Herrmann

5531 S. W. Key

5531 H. S. Lauson

5531 S. T. Montgomery

5531 H. S. Morgan

5532 W. R. Wawersik (15)

5532 D. W. Hannum

5820 R. E. Whan

5821 R. W. Bild

3141 T. L. Werner (5)

3151 W. L. Garner (3)

3154-3 R. P. Campbell (25)

For DOE/TIC

8266 E. A. Aas